Progress in Natural Science: Materials International 32 (2022) 786–792

HOSTED BY

Contents lists available at ScienceDirect

Progress in Natural Science: Materials International

journal homepage: www.elsevier.com/locate/pnsmi

# Ultrafastly activated needle coke as electrode material for supercapacitors

Cuihua Zeng[a], Cunpeng Duan[a], Zhaoxin Guo[a], Zhedong Liu[a], Shuming Dou[a], Qunyao Yuan[a], Peng Liu[b], Jingchao Zhang[a], Jiawei Luo[a], Weidi Liu[c], Jinfeng Zhang[a,**], Yanan Chen[a,*], Wenbin Hu[a,***]

[a] *School of Materials Science and Engineering, Tianjin University, Tianjin, 300072, China*
[b] *Institute of Frontier and Interdisciplinary Science and Key Laboratory of Particle Physics and Particle Irradiation (MOE), Shandong University, Qingdao, Shandong, 266237, China*
[c] *Australian Institute for Bioengineering and Nanotechnology, The University of Queensland, St Lucia, 4072, QLD, Australia*

ARTICLE INFO

*Keywords:*
Supercapacitors
Activated porous carbons (APCs)
High temperature shock (HTS) method
Cost-effective

ABSTRACT

The uniform porous structure makes activated porous carbons (APCs) superior electrode material. Traditionally, APCs are produced by a combination of time-consuming high-temperature heat treatment and activation, with a production time of up to several hours. The produced APCs have relatively low specific surface area (SSA) and porosity. Therefore, the electrochemical performance is poor, which limits its application in high-power energy storage devices. Here, APCs materials are directly synthesized by a high temperature shock (HTS) strategy using needle coke as a precursor. The structure of as-prepared APC is characterized by XRD, SEM and Raman, and electrochemical tests confirmed its good electrochemical performance. In the two-electrode system, the supercapacitor with HTS-APC as the electrode material provides a high energy density of 35 Wh kg$^{-1}$ and a high power density of 875 W kg$^{-1}$ in EMIMBF$_4$ ionic liquid. This work is instructive for the rapid synthesis of electrode materials, and also provides guidance for the large-scale application of porous carbon materials.

## 1. Introduction

In order to achieve the goals of "carbon peak" and "carbon neutrality", we need to reduce the use of fossil energy and renewable energy is becoming increasingly important [1–3]. Generally speaking, renewable energy industry can be separated the following three stages: production, storage and utilization [4]. The key challenges to achieve industrialization are energy storage and efficiency [5,6]. Secondary batteries and supercapacitors (SCs) for energy storage have received increasing attention [7]. It is widely known that the energy density of SCs is limited [5,8] while the fast-charging mechanism allows SCs to store enough energy within a short period of time. In addition, more charge-discharge cycles compared with rechargeable batteries makes them more promising for energy storage [5]. In addition, SCs also have the advantages of eco-friendliness, high capacitance and good storage capacity [9,10]. Correspondingly, they have a wide range of applications in industry, military, and automotive. Based on different energy storage mechanisms, SCs can be divided into electrodynamic double-layer capacitors (EDLCs) and pseudocapacitors [10–12]. For EDLCs, the performance of capacitor mainly depends on the electric double layer, and the capacitor use the electric double layer formed at the interface between the liquid electrolyte and the solid electrode for charge storage. Because the distance between the two charge layers is very small (generally below 0.5 nm), and the special electrode structure is adopted, the surface area of the electrode is increased ten thousand times, resulting in a significantly high capacitance [6,13,14]. The physicochemical properties of electrode materials largely determine the electrochemical performance of supercapacitors. Electrode materials for SCs mainly consist of three types: (1) carbon materials (2) conducting polymers (3) metal oxides/hydroxides [11,15]. Carbon-based materials are the most widely studied and applied materials in capacitor industrialization [5] due to its high chemical/thermal stability and excellent electrical conductivity [5,6,10,16].

For carbon materials, nano engineering can greatly influence their properties. Porous carbons with the advantages, such as high specific surface area, high electrical conductivity, excellent cycle stability, and low price, are widely used as electrode materials for EDLCs [16–18]. The

---

[*] Corresponding author.
[**] Corresponding author.
[***] Corresponding author.

*E-mail addresses:* jinfeng@tju.edu.cn (J. Zhang), yananchen@tju.edu.cn (Y. Chen), wbhu@tju.edu.cn (W. Hu).

https://doi.org/10.1016/j.pnsc.2022.10.008
Received 28 September 2022; Received in revised form 19 October 2022; Accepted 25 October 2022

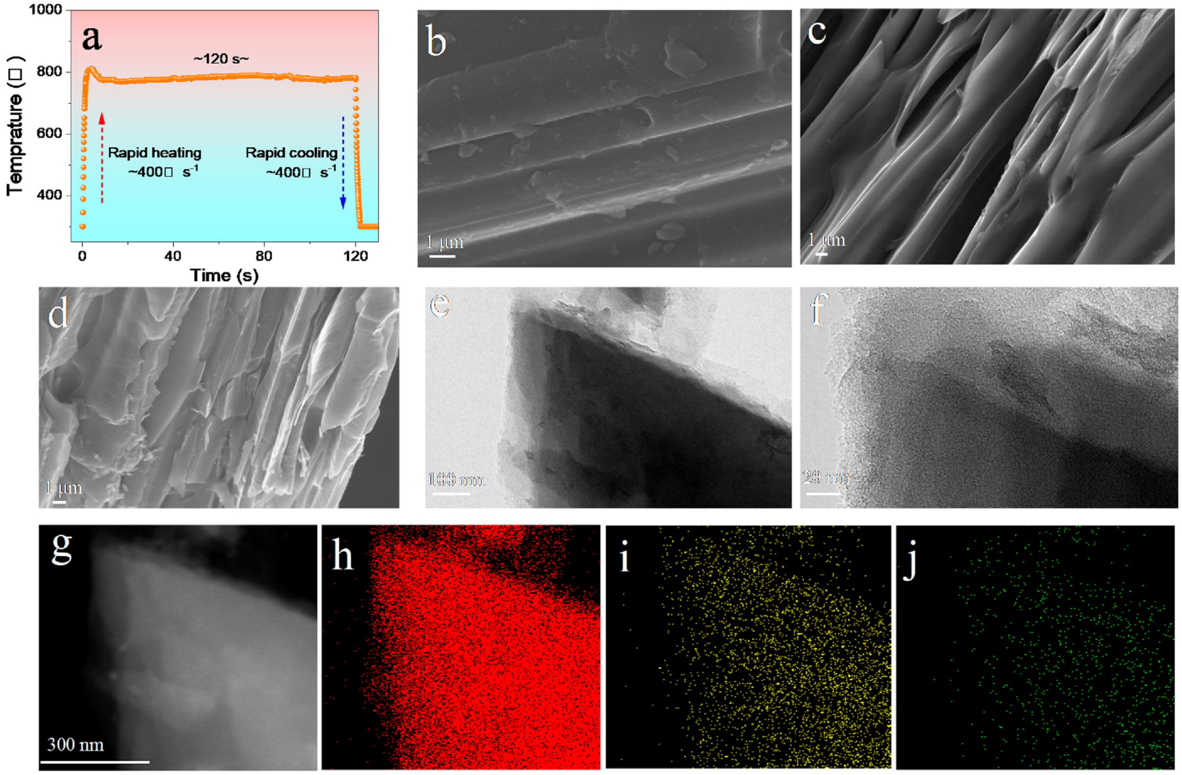

**Fig. 1.** a) HTS test curve exhibits the heating and cooling rates as ~400 and 400 °C $s^{-1}$, respectively. b-d) SEM images of Raw material needle coke, HTS-APC and TF-APC, e) TEM image of HTS-APC, f) High-resolution TEM image of HTS-APC with abundant micropores. g-j) EDS mapping of HTS-APC.h) C element, i) O element, j) N element.

porous structure provides shorter diffusion paths for ion/electron transport, increases active sites for ion storage and reduces stress-induced volume change [19]. The raw materials for the preparation of porous carbon materials are extremely wide, ranging from minerals, wood to synthetic materials [17,20]. The electrochemical performance of porous carbon materials is related to the specific surface area [21], pore size distribution [22,23] and surface functional groups [24–26]. Porous carbon materials with different properties can be prepared by selecting suitable carbonaceous precursors. Needle coke is a kind of high-quality coke produced by pretreatment and delayed coking of aromatic-rich heavy oil [19,27]. It has a special layered structure, excellent electrical conductivity and chemical stability. In addition, Needle coke has 95% carbon content, low ash content, low volatility and strong anti-oxidative stability [7,27,28], which is an ideal precursor for the preparation of porous carbon. The three-dimensional structure of needle coke with well-connected pores can not only provide continuous channels, ensure good contact with electrolytes, but also accelerate charge transfer by reducing diffusion pathways [23,24,29]. During the preparation process of porous carbon, non-carbon components in the carbon-containing raw materials are lost in the form of volatile components at high temperature, and a certain amount of carbon in the raw materials will be consumed to generate a large number of micro-pore structure. The synthesis of porous carbon electrode materials consists of activation and carbonization processes [30,31]. At present, the activation of porous carbon is mostly accomplished by physical activation of heat treatment for more than 10 h, or chemical activation of heat treatment for several hours [31–33]. Synthesizing carbon materials with robust cycle stability and high-energy-density in a simple, fast and cost-effective method remains challenging in industry [34].

In this study, activated porous carbon is synthesized by rapid high temperature shock (HTS) strategy under vacuum conditions using needle coke as the precursor and KOH as the activator [35]. Instantaneous heating (heating rate ≈ 400 °C $s^{-1}$) and rapid cooling induce uniform porous structure. The reaction is controlled to be completed within 10 s, which greatly shortens the production time of activated porous carbon (APC) so improves the production efficiency. The porous carbon synthesized by the HTS strategy exhibits good electrochemical performance. This work uses a facile and efficient way to synthesize high-performance APCs, which presents a new method for the rapid synthesis of high-performance electrode materials. The HTS strategy can extensively contribute to the large-scale production and application of APCs.

## 2. Experimental section

### 2.1. Material synthesis

The purchased needle cokes are manually ground into more uniform particles in a mortar. The needle coke particles are further ground by a ball mill to obtain fine needle coke powders. The obtained needle coke powder is processed as follow: Weigh 3 g of KOH medicine in a beaker. Add 10 mL of distilled water into the beaker, and stir until the KOH is completely dissolved and form a colorless and transparent solution. The needle coke powder is added into the KOH aqueous solution to mix uniformly by ultrasonic for 15 min, and finally the slurry can be obtained. The obtained slurry is subjected to HTS treatment (the thermal shock temperature is 750–800 °C) as follow: The carbon cloth is connected by two electrodes (the mixed slurry with KOH is uniformly loaded on carbon cloth), and the needle coke powder is thermally shocked by the HTS equipment. The current and time of the HTS equipment are set as 15 A and 120 s, respectively. The coke porous carbon powder is cleaned, suction filtered, dried at 60 °C for 12 h under vacuum, and finally HTS-APC can be obtained. TF-APC is calcined at 800 °C for 2 h in argon atmosphere.

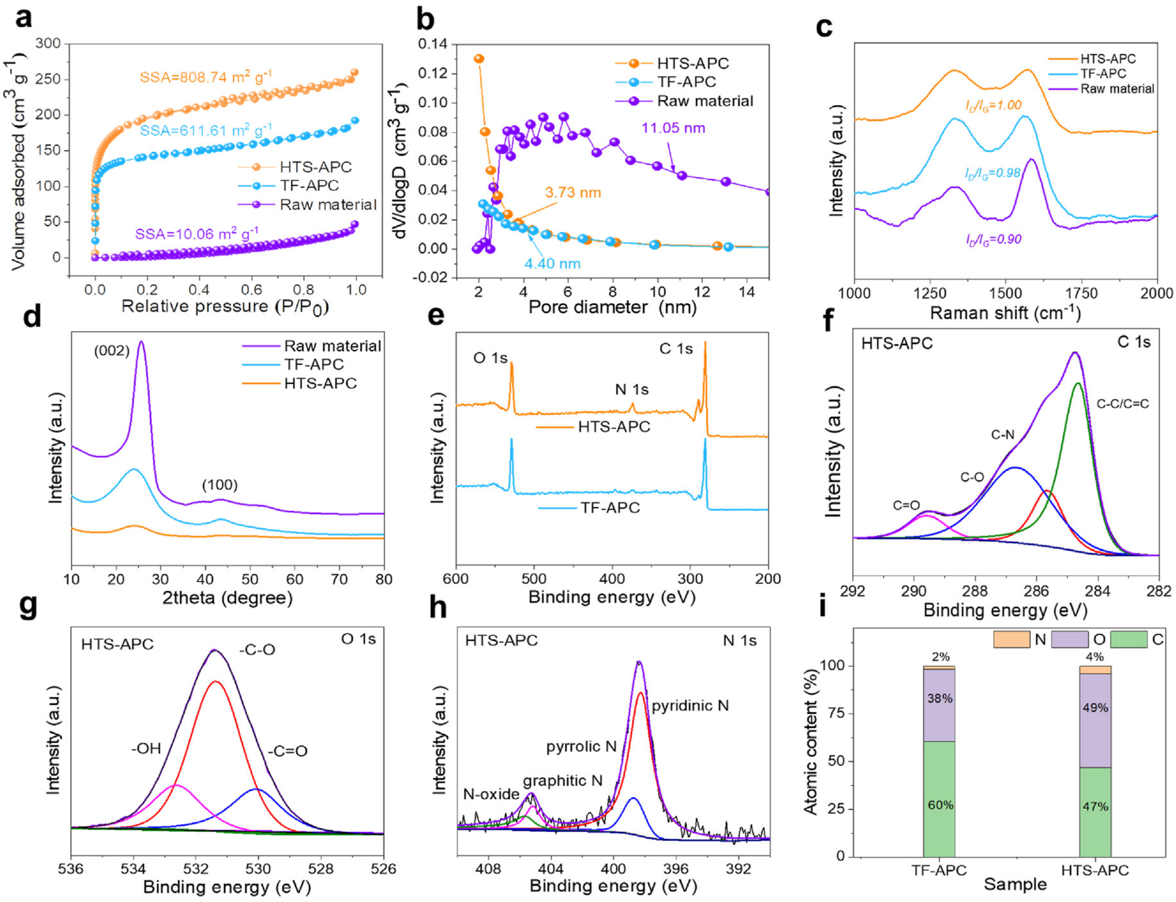

**Fig. 2.** Physical characterization of activated porous carbons (HTA-APC, TF-APC, Raw material needle coke). a, b) Nitrogen adsorption-desorption isotherms and pore size distribution curves of HTS-APC, TF-APC and Raw material needle coke, c) Raman spectrum, d) X-ray diffractometer (XRD) patterns, e) XPS survey, f-h) Deconvolution curves of C1s, O1s, N1s, i) Surface atomic content of HTS-APC, TF-APC, Raw material.

### *2.2. Material characterization*

The crystal structure of all samples are evaluated using a Bruker (Cu Kα radiation diffractometer, λ = 1.5406 Å) D8 advanced X-ray diffractometer with working voltage 40 KV and working current 40 mA. Raman (Jobin-Yvon HR 800) spectroscopy is used for scattering and measuring structural properties. The TEM and HRTEM images of samples mentioned are obtained by JEM-2100F and JEM-ARM200F (accelerating voltage: 200 kV), respectively. Scanning electron microscopy (SEM) and energy dispersive spectroscopy (EDS) are performed with a JEOL JSM-7800F microscope to obtain the sample morphology and element distribution. X-Ray photoelectron spectroscopy (XPS) measurements are performed with an ESCALAB 250Xi X-ray photoelectron spectrometer from Thermo Fischer, USA, with Al Kα (hν = 1486.6 eV) as the radiation source (C 1s = 284.8 eV). The BET surface area and pore size distribution are tested using $N_2$ adsorption/desorption experiments.

### *2.3. Electrochemical measurement*

In a three-electrode system, the electrochemical properties of HTS-APC are explored using 6 mol $L^{-1}$ KOH aqueous solution as electrolyte. The electrode is made up of 80% active cathode material HTS-APC, 10% Super P as conductive agent and 10% Polytetrafluoroetylene (PTFE) as binder, mixing with ethanol to form a slurry, which is coated on the foamed nickel current collector (1 × 1 $cm^2$). The electrode material is then vacuum dried overnight, and the amount of active material loaded in the single electrode is ~1.0 mg $cm^{-2}$. The platinum and Hg/HgO electrodes correspond to the counter and reference electrodes in the three-electrode system. Using cyclic voltammetry (CV), galvanostatic charge-discharge (GCD), and electrochemical impedance spectroscopy (EIS) obtain capacitive performance of samples.

In the two-electrode test, the button-type supercapacitor is assembled from CR2032 with cellophane fibers for the separator, with active material loading of ~1.0 mg $cm^{-2}$ and ~2.0 mg $cm^{-2}$ in 6 mol $L^{-1}$ KOH and $EMIMBF_4$ electrolytes, respectively. The voltages for GCD and CV measurements are set to 0–1.0 V and 0–3.5 V. The specific mass specific capacitance, specific energy density and specific power density are calculated as follows:

$$C_s = \frac{I \times \Delta t}{m \times \Delta V} \tag{1}$$

$$C_t = \frac{2 \times I \times \Delta t}{m \times \Delta V} \tag{2}$$

$$E = \frac{1}{2} C_t \Delta V^2 \times \frac{1000}{3600} \times \frac{1}{4} \tag{3}$$

$$P = \frac{3600 \times E}{\Delta t} \tag{4}$$

where $C_s$ denotes the specific capacitance of single electrode , $C_t$ represents the specific capacitance in a two electrode system. where and $I$, $\Delta t$, $m_1$, $\Delta V$ refer to current density (A $g^{-1}$), the mass of UAPC (g), the discharge time (s), $\Delta V$ shows voltage window (V).

## 3. Results and discussion

Fig. 1a shows the variation of temperature as a function of time

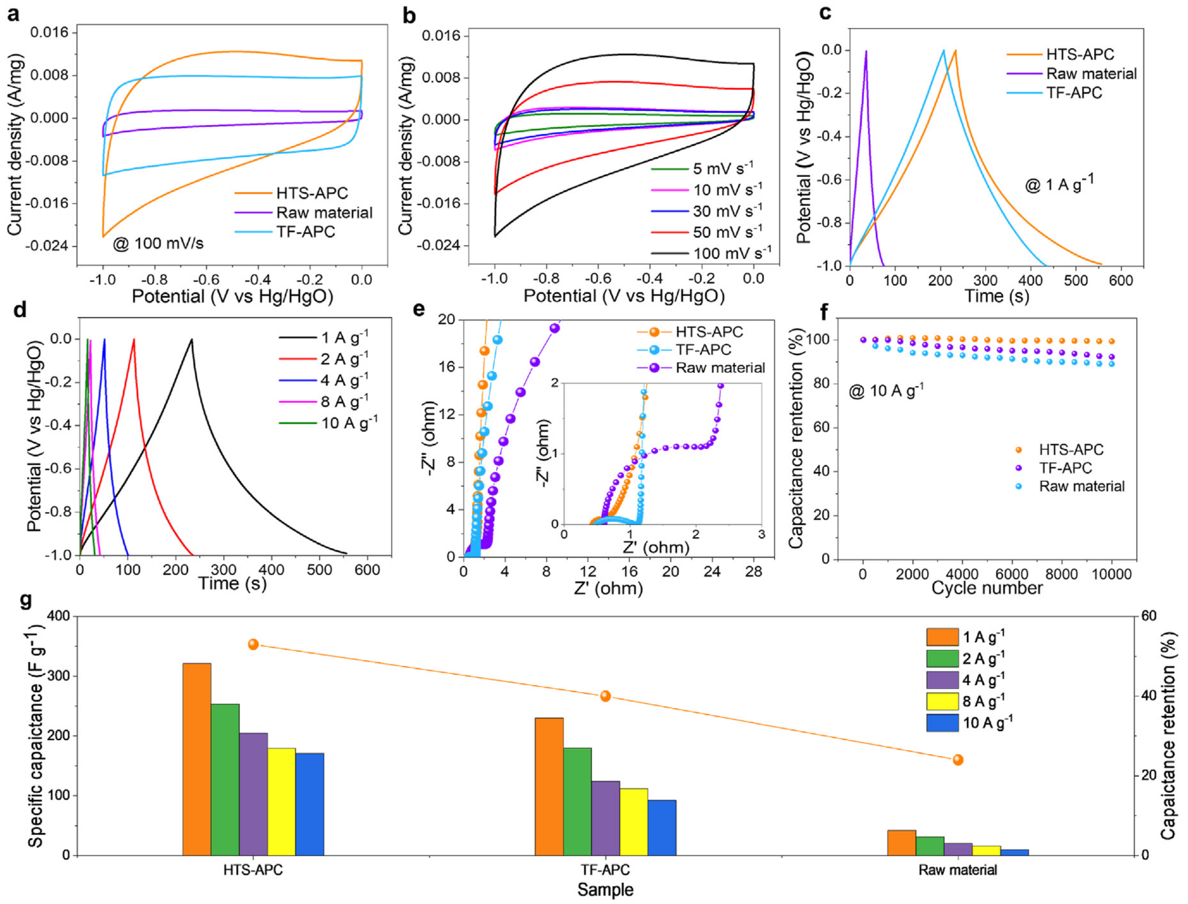

**Fig. 3.** The electrochemical properties of HTS-APC, TF-APC and Raw material needle coke. a) Cyclic voltammetry curve (CV) curves of HTS-APC, TF-APC, Raw material at 100 mV $s^{-1}$, b) CV curves of HTS-APC from 5 to 100 mV $s^{-1}$, c) Galvanostatic charge–discharge (GCD) curves of HTS-APC, TF-APC, Raw material at 1 A $g^{-1}$, d) GCD curves of HTS-APC at various current density, e) Nyquist plot, f) cycling stability at 10 A $g^{-1}$, and g) The mass specific capacitance versus different current densitie

during the HTS process. The rapid heating leads to the increased temperature at the speed of 400 °C $s^{-1}$, and a short holding time of 120 s is sufficient to finalize the reaction. The fast HTS technique offers the unique advantages of highly efficient and ultrafast manufacturing compared with the traditional time-consuming, inefficient tube furnace fabrication [35–37]. The morphology of the needle coke raw material exhibits a typical streamlined sheet-like structure as shown in Fig. 1b. Fig. 1c presents the basic morphology of HTS-APC after rapid KOH activation. As can be seen, comparing with the raw material, the HTS-APC exhibits several crevices with uniform and dense folds on the surface, which largely elevates the specific surface area of carbon materials. Needle char APC produced in tube furnace similarly shows obvious crevices and delamination under various sizes of surface folds, which limit its specific surface area and pore generation (as shown in Fig. 1d). The TEM images in Fig. 1e and f demonstrate the pore structure of HTS-APC also exhibits the obvious layered structure characteristic. In the EDS mapping (Fig. 1g), homogeneous elemental distribution of HTS-APC can be observed.

$N_2$ adsorption-desorption curves (Fig. 2a and b) explain the physical properties of the pore structures of the three samples. The adsorption-desorption curves of HTS-APC exhibit combined isotherms of type I and type IV with hysteresis loops. At relatively low pressure ($P/P_0 < 0.2$), the presence of high-quality micropores corresponds to a period of sharp increase in isotherm. The existence of the mesopore can be confirmed by the hysteresis loop of the capillary condensation process under moderate relative pressure (the range of $P/P_0$ is 0.4–0.8). In addition, the macropore can be demonstrated by a slight rise in the curve at high relative pressure (the range of $P/P_0$ is 0.9–1.0). It can be observed that HTS-APC demonstrates the highest specific surface area among the three samples as shown in Fig. 2a [38–40]. Fig. 2b shows the pore size distribution obtained by micromeritic automatic analyzer. It can be observed that HTS-APC possesses smaller average pore size than TF-APC and raw material. The curve shape of HTS-APC proves that most of the pores are micropore and mesopore, which can provide sufficient adsorption active sites and fast transport channels for ions. The pore structure endows HTS-APC with excellent capacitive performance [38,41,42]. Fig. 2c shows the Raman spectra of the three samples, in which the G band at ~1580 $cm^{-1}$ and the D band at ~1350 $cm^{-1}$ representing the characteristic carbon, the graphitic disorder and defect levels of the graphitic layer, respectively [43,44]. Among them, the peak intensities ($I_D/I_G$) of the D and G bands can be used to evaluate the degree of graphitization. As shown, the HTS-APC possesses the highest peak intensity ratio ($I_D/I_G = 1.00$), which proves the highest disorder and richest defect characteristics [45]. From the XRD patterns (Fig. 2d), it can be seen that HTS-APC exhibits a narrower (002) peak half-width compared to the other two samples, corresponding to a richer degree of defects and a higher degree of disorder. In addition, the lower intensity of the (002) peak also indicates a lower level of graphitization, consistent with the Raman analysis [43,46]. Based on the XPS full spectra of HTS-APC and TF-APC as in Fig. 2e, the presence of C, O peaks can be clearly observed with weak peak intensity of N. Fig. 2f–h shows high-resolution XPS spectra of C, O and N elements of the HTS-APC sample. The C 1 s spectrum is fitted to five individual peaks including C–C/C═C (~284.8 eV), C–N (~285.7 eV), C–O (~286.8 eV) and C═O (~289.6 eV) as shown in Fig. 2f. In Fig. 2g, The O 1 s spectrum can be fitted to three peaks corresponding to C═O (~530.0 eV), C–O (~531.4 eV), and –OH (~532.6

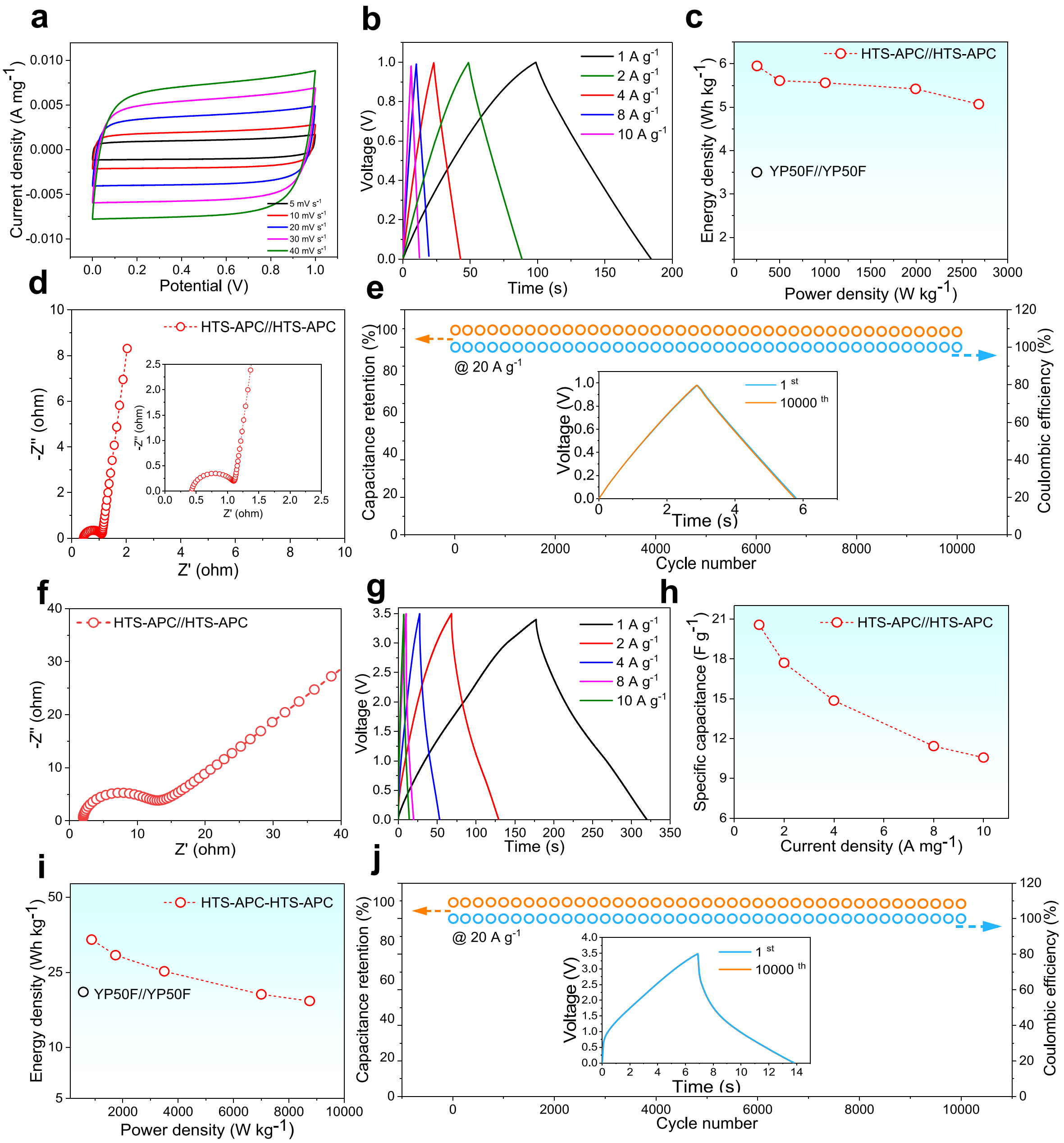

**Fig. 4.** The electrochemical properties of HTS-APC. a-e) HTS-APC//HTS-APC is tested in 6 M KOH electrolyte, f-j) HTS-APC//HTS-APC is tested in EMIMBF4 electrolyte. a) CV curves at 5 mV $s^{-1}$ to 40 mV $s^{-1}$, b) GCD curves at 1 A $g^{-1}$ to 10 A $g^{-1}$, c) Ragone plot, d) Nyquist plot, e) Cycling stability of HTS-APC//HTS-APC at 10 A $g^{-1}$, f) Nyquist plot, g) GCD curves at 1 A $g^{-1}$ to 10 A $g^{-1}$, h) The mass specific capacitance versus different current densities, i) Ragone plot, j) Cycling stability of HTS-APC//HTS-APC at 20 A $g^{-1}$.

eV). The four peaks located at ~398.3, ~398.8, ~405.1 and ~405.7 eV in Fig. 2h belong to pyridinic N, pyrrolic N, graphitic N, N-oxide (obtained from N 1s spectral deconvolution), respectively [41,43,47]. Fig. 2i shows the relative contents of N, O, and C in different samples. It can be clearly found that the content of N and O elements in sample HTS-APC (4% and 49%) is significantly higher than that of TF-APC (2% and 38%), indicating the surface tension and wettability of the electrode surface of the HTS-APC are better than TF-APC [48]. Additionally, the preparation method of HTS is more efficient, faster as well as lower cost [35,49].

The electrochemical performance of the three samples is investigated using three-electrode system in 6 mol $L^{-1}$ KOH electrolyte. The CV curves of the three samples at a scan rate of 100 mV $s^{-1}$ are shown in Fig. 3a. It can be seen that HTS-APC possesses the highest absolute integral area, indicating the largest specific capacitance. In Fig. 3b, the shape of CV curves of the HTS-APC sample maintains a good rectangle shape from 5 to 100 mV $s^{-1}$, indicating that the material exhibits excellent charge transfer kinetics. Fig. 3c shows the GCD curves of the three samples all show triangular shape, proving that the three samples have typical EDLC characteristics and good reversible charge-discharge behavior. In addition, HTS-APC also exhibits a longer discharge time, exhibiting the best specific capacitance at 1 A $g^{-1}$. Fig. 3d shows that the shape of the GCD curves of the HTS-APC samples at different current densities, which are all triangular-like, proving that the rate performance is satisfactory. The Nyquist curve of Fig. 3e consists of a small semicircle in the high frequency region and a steep slope in the low frequency region, which indicates an approximately ideal capacitive behavior and low equivalent series resistance [50,51]. It can be observed in the Nyquist plot that HTS-APC exhibits the smallest equivalent series resistance, indicating the highest rate performance among the three samples. Fig. 3f shows the cycle rate performance of the three samples after 10,000 cycles in 10 A $g^{-1}$. It can be observed that HTS-APC possesses the highest capacity retention (99.34%), which is significantly higher than TF-APC (92.28%) and raw material (89.06%). HTS-APC exhibits a high mass specific capacitance of 326 F $g^{-1}$ at 1 A $g^{-1}$ (Fig. 4g). Furthermore, the specific capacitance value reaches 171 F $g^{-1}$ even at a high current density of 10 A $g^{-1}$, indicating excellent rate characteristics superior to both TF-APC and raw material. This proves that the needle coke porous carbon manufactured by HTS technique shows a good application prospect for electrochemical energy storage when apply in supercapacitors.

The electrochemical energy storage performance of HTS-APC material in supercapacitor is investigated (using 6 M KOH and $EMIMBF_4$ ionic liquid as electrolytes). The CV curves of HTS-APC//HTS-APC in KOH electrolyte all exhibit regular rectangles (the scan rate is increased from 5 mV $s^{-1}$ to 40 mV $s^{-1}$), demonstrating that HTS-APC//HTS-APC possesses EDLC properties as shown in Fig. 4a. Fig. 4b shows that HTS-APC//HTS-APC exhibits a triangular shape in GCD curves at different current densities, confirming its excellent rate capability. Fig. 4c shows the Ragone plot of HTS-APC//HTS-APC (KOH as electrolyte) which performs better than YP50F//YP50F [35]. The mass specific capacitance at different current densities in KOH are shown in Fig. S1a. The Nyquist plot of HTS-APC//HTS-APC as shown in Fig. 4d. It can be seen that HTS-APC//HTS-APC exhibits smaller charge transfer resistance ($R_{ct}$) and internal resistance ($R_s$), indicating that the supercapacitor performs higher electrode conductivity and outstanding electron transport rate. From Fig. S1b, it can be seen that the Bode phase angle is 83.9° at low frequency region, indicating that the capacitive reactance is zero. It can also be noted that the time constant $\tau_0$ is merely 0.28 s, indicating the excellent energy storage and transport capabilities of the HTS-APC//HTS-APC supercapacitor. The impedance amplitude in the high frequency region is relatively stable and decreases with increasing the frequency. The impedance magnitude tends to zero, which correlates to the extremely low resistance of HTS-APC//HTS-APC supercapacitors in KOH. Moreover, the cycle stability test proves that HTS-APC//HTS-APC still maintains 99.16% of specific capacitance and nearly 100% of the coulombic efficiency after 10,000 cycles at 20 A $g^{-1}$, exhibiting superior cycle rate characteristics (Fig. 4e). The analysis of the Nyquist plot of HTS-APC//HTS-APC in Fig. 4f is consistent with Fig. 4d in $EMIMBF_4$ ionic liquid electrolyte. It can be seen from Fig. S2 that the voltage window of HTS-APC//HTS-APC is increased to 3.5 V in $EMIMBF_4$ electrolyte, and the CV curves still shows a rectangular shape. In addition, the GCD curve with triangular shape shown in Fig. 4g indicates the excellent rate characteristics of HTS-APC//HTS-APC supercapacitor. Fig. 4h shows that the mass specific capacitances of the supercapacitors at current densities of 1–10 A $g^{-1}$ are 20.6, 17.7, 14.9, 11.4, 10.6 F $g^{-1}$, respectively. In Fig. 4i, the energy density of HTS-APC//HTS-APC reaches 35 Wh $kg^{-1}$ when the power density is 875 W $kg^{-1}$. The energy density remains at 17.9 Wh $kg^{-1}$ when the power density is 8748 W $kg^{-1}$. These results indicate that HTS-APC//HTS-APC as a supercapacitor can provide an energy density exceeding that of supercapacitors prepared from commercial activated carbon YP50F [35], and exhibit an ideal application prospect. Moreover, the capacitance retention (98.81%) and the Coulomb efficiency (100%) of HTS-APC//HTS-APC after 10,000 cycles at 20 A $g^{-1}$ demonstrates outstanding cycle stability of the needle coke porous carbon manufactured by HTS carbonization and activation technique.

## 4. Conclusion

In summary, we successfully synthesize a porous carbon material with needle coke as a precursor using a HTS strategy, and confirm its application potential as an electrode material for supercapacitors [52,53]. During the HTS process, KOH is fully contacted with needle coke to fully activate it, which simultaneously produce a large amount of carbon dioxide and other gases. The HTS technique contributes to the synthesis of the porous carbon structure. In addition, benefitting from the characteristics of rapid heating and cooling and short-term heat preservation, the size of the pore structure is relatively uniform and suitable. The results show that needle coke is a suitable precursor for the preparation of porous carbon materials, which can withstand the activation process. The porous carbons prepared by HTS show large specific surface area, suitable pore size distribution and three-dimensional bulk structure, which can provide the best path for ion transport. In a two-electrode system using 6 M KOH solution as the electrolyte, the HTS-APC exhibits the capacitance retention rate is 99.16% for 10,000 cycles at 20 A $g^{-1}$. In a two-electrode system using $EMIMBF_4$ as the electrolyte, the energy density of HTS-APC//HTS-APC reaches 35 Wh $kg^{-1}$ when the power density is 875 W $kg^{-1}$. The performance of APC prepared by HTS method is better than that prepared by traditional method, and also better than that of commercial sample YP50F. APC is not only be used in energy storage devices but also has broad application prospects in the fields of catalysis and harmful gas adsorption. HTS has the advantages of fast, efficient and economical production of APC, which provides a new method for the preparation of APC and promotes the development of APC towards a more efficient and eco-friendly aspect.

## Declaration of competing interest

The authors declare that they have no known competing financial interests or personal relationships that could have appeared to influence the work reported in this paper.

## Acknowledgements

Contributed equally to this work. The authors acknowledge the financial support from the National Natural Science Foundation of China (52171219, 91963113).

## Appendix A. Supplementary data

Supplementary data to this article can be found online at https://doi.org/10.1016/j.pnsc.2022.10.008.

## References

[1] Q. Zhu, D. Zhao, M. Cheng, J. Zhou, K.A. Owusu, L. Mai, Y. Yu, Adv. Energy Mater. 9 (36) (2019).

[2] J. Zhang, Z. Liu, C. Zeng, J. Luo, Y. Deng, X. Cui, Y. Chen, Rare Met. 65 (2022) 2613–2626.

[3] J. Zhang, J. Wen, W. Liu, X. Cui, Y. Chen, Sci. Chin. Mater. 65 (10) (2022) 2613–2626.

[4] C.J. Raj, R. Manikandan, M. Rajesh, P. Sivakumar, H. Jung, S.J. Das, B.C. Kim, J. Power Sources 490 (2021).

[5] S.S. Shah, E. Cevik, M.A. Aziz, T.F. Qahtan, A. Bozkurt, Z.H. Yamani, Synth. Met. 277 (2021).

[6] D.T. Pham, F. Yao, Y.H. Lee, ChemSusChem 8 (2015) 2284–2311.

[7] J. Cheng, Z. Lu, X. Zhao, X. Chen, Y. Zhu, H. Chu, Carbon Lett. 31 (1) (2020) 57–65.

[8] X. Huang, L. Gou, L. Yang, J. Alloys Compd. 786 (2019) 91–97.

[9] B. Zhang, Q. Liu, K. Xu, R. Zou, C. Wang, Prog. Nat. Sci.: Mater. Int. 32 (2) (2022) 163–170.

[10] S.S. Shah, M.A. Alfasane, I.A. Bakare, M.A. Aziz, Z.H. Yamani, J. Energy Storage 30 (2020).

[11] B. Liu, Z. Cao, Z. Yang, W. Qi, J. He, P. Pan, H. Li, P. Zhang, Prog. Nat. Sci.: Mater. Int. 32 (1) (2022) 10–19.

[12] G.Z. Chen, Prog. Nat. Sci.: Mater. Int. 31 (6) (2021) 792–800.

[13] S. Wu, Y. Chen, T. Jiao, J. Zhou, J. Cheng, B. Liu, S. Yang, K. Zhang, W. Zhang, Adv. Energy Mater. 9 (47) (2019).

[14] S. Kumar, G. Saeed, L. Zhu, K.N. Hui, N.H. Kim, J.H. Lee, Chem. Eng. J. 403 (2021).

[15] R. Zhang, W. Zhang, M. Shi, H. Li, L. Ma, H. Niu, Dyes Pigments 199 (2022).

[16] Z. Shang, X. An, H. Zhang, M. Shen, F. Baker, Y. Liu, L. Liu, J. Yang, H. Cao, Q. Xu, H. Liu, Y. Ni, Carbon 161 (2020) 62–70.

[17] J. Cheng, Z. Lu, X. Zhao, X. Chen, Y. Liu, J. Power Sources 494 (2021).

[18] J. Xu, X. Wang, X. Zhou, N. Yuan, S. Ge, J. Ding, Electrochim. Acta 301 (2019) 478–486.

[19] W. Ren, Z. Zhang, Y. Wang, G. Kan, Q. Tan, Z. Zhong, F. Su, RSC Adv. 5 (15) (2015) 11115–11123.

[20] H. Zhang, C. Ma, Y. Hu, A. Maclennan, B. Hu, J. Zhao, T. Wang, C. Cheng, J. Solid State Electrochem. 20 (12) (2016) 3437–3445.

[21] A.G. Pandolfo, A.F. Hollenkamp, J. Power Sources 157 (1) (2006) 11–27.

[22] H. Zhang, G. Cao, Y. Yang, Z. Gu, Carbon 46 (1) (2008) 30–34.

[23] L. Qie, W. Chen, H. Xu, X. Xiong, Y. Jiang, F. Zou, X. Hu, Y. Xin, Z. Zhang, Y. Huang, Energy Environ. Sci. 6 (8) (2013).
[24] Z. Chen, X. Wang, B. Xue, W. Li, Z. Ding, X. Yang, J. Qiu, Z. Wang, Carbon 161 (2020) 432–444.
[25] J.E. Zuliani, S. Tong, C.Q. Jia, D.W. Kirk, J. Power Sources 395 (2018) 271–279.
[26] Y. Liu, J. Yao, G. Li, Mater. Lett. 266 (2020).
[27] Y. Zhong, L. Xu, C. Li, B. Zhang, W. Wu, Carbon 153 (2019) 602–608.
[28] D. Zhao, H. Zhao, J. Ye, W. Song, S. Miao, H. Shen, Y. Zhao, M. Kang, Z. Li, Electrochim. Acta 329 (2020).
[29] H. Jiang, P.S. Lee, C. Li, Energy Environ. Sci. 6 (1) (2013) 41–53.
[30] A. Gopalakrishnan, S. Badhulika, J. Power Sources 480 (2020).
[31] X. Liang, R. Liu, X. Wu, Microporous Mesoporous Mater. 310 (2021).
[32] M. Shang, J. Zhang, X. Liu, Y. Liu, S. Guo, S. Yu, S. Filatov, X. Yi, Appl. Surf. Sci. 542 (2021).
[33] Q. Wang, F. Liu, Z. Jin, X. Qiao, H. Huang, X. Chu, D. Xiong, H. Zhang, Y. Liu, W. Yang, Adv. Funct. Mater. 30 (39) (2020).
[34] S.S. Shah, H.T. Das, H.R. Barai, M.A. Aziz, Polymers 14 (2) (2022).
[35] Z. Liu, C. Duan, S. Dou, Q. Yuan, J. Xu, W.D. Liu, Y. Chen, Small 18 (23) (2022), e2200954.
[36] S. Liu, Y. Shen, Y. Zhang, B. Cui, S. Xi, J. Zhang, L. Xu, S. Zhu, Y. Chen, Y. Deng, W. Hu, Adv. Mater. 34 (2) (2022), e2106973.
[37] S. Liu, Z. Hu, Y. Wu, J. Zhang, Y. Zhang, B. Cui, C. Liu, S. Hu, N. Zhao, X. Han, A. Cao, Y. Chen, Y. Deng, W. Hu, Adv. Mater. 32 (48) (2020), e2006034.
[38] L. Zhao, L.Z. Fan, M.Q. Zhou, H. Guan, S. Qiao, M. Antonietti, M.M. Titirici, Adv. Mater. 22 (45) (2010) 5202–5206.
[39] D. Dong, Y. Zhang, Y. Xiao, T. Wang, J. Wang, C.E. Romero, W.P. Pan, J. Colloid Interface Sci. 580 (2020) 77–87.
[40] S. Ghosh, R. Sarathi, S. Ramaprabhu, J. Colloid Interface Sci. 539 (2019) 245–256.
[41] X. Jing, L. Wang, K. Qu, R. Li, W. Kang, H. Li, S. Xiong, ACS Appl. Energy Mater. 4 (7) (2021) 6768–6776.
[42] F. Chen, C. Liu, B. Cui, S. Dou, J. Xu, S. Liu, H. Zhang, Y. Deng, Y. Chen, W. Hu, J. Power Sources 482 (2021).
[43] J. Zou, P. Liu, L. Huang, Q. Zhang, T. Lan, S. Zeng, X. Zeng, L. Yu, S. Liu, H. Wu, W. Tu, Y. Yao, Electrochim. Acta 271 (2018) 599–607.
[44] S. Maruyama, T. Fukutsuka, K. Miyazaki, T. Abe, Electrochim. Acta 265 (2018) 41–46.
[45] Y. Wang, Y. Liu, D. Wang, C. Wang, L. Guo, T. Yi, Appl. Surf. Sci. 506 (2020).
[46] W. Zhang, C. Yu, L. Chang, W. Zhong, W. Yang, Electrochim. Acta 282 (2018) 642–652.
[47] B. Duan, X. Gao, X. Yao, Y. Fang, L. Huang, J. Zhou, L. Zhang, Nano Energy 27 (2016) 482–491.
[48] G. Ni, F. Qin, Z. Guo, J. Wang, W. Shen, Electrochim. Acta 330 (2020).
[49] R. Jiang, Y. Da, Z. Chen, X. Cui, X. Han, H. Ke, Y. Liu, Y. Chen, Y. Deng, W. Hu, Adv. Energy Mater. 12 (8) (2022).
[50] T. Shang, Y. Xu, P. Li, J. Han, Z. Wu, Y. Tao, Q.H. Yang, Nano Energy 70 (2020).
[51] T. Liu, Z. Zhou, Y. Guo, D. Guo, G. Liu, Nat. Commun. 10 (1) (2019) 675.
[52] Y. Chen, Y. Wang, S. Zhu, K. Fu, X. Han, Y. Wang, B. Zhao, T. Li, B. Liu, Y. Li, J. Dai, H. Xie, T. Li, J.W. Connell, Y. Lin, L. Hu, Mater. Today 24 (2019) 26–32.
[53] Y. Chen, Y. Li, Y. Wang, K. Fu, V.A. Danner, J. Dai, S.D. Lacey, Y. Yao, L. Hu, Nano Lett. 16 (9) (2016) 5553–5558.